narra j

**Original Article**

# Development and evaluation of a synthetic Cu-Zn-reinforced biphasic calcium phosphate scaffold for periodontal bone repair

**Devina Novelia[1], Theophani O. Cahyadi[1], Natasya MP. Sidharta[1], Mora Octavia[2*], Evi UM. Situmorang[3] and Daniel Edbert[4]**

[1]School of Medicine and Health Sciences, Atma Jaya Catholic University of Indonesia, Jakarta, Indonesia; [2]Department of Dental Medicine, School of Medicine and Health Sciences, Atma Jaya Catholic University of Indonesia, Jakarta, Indonesia; [3]Department of Physiology, School of Medicine and Health Sciences, Atma Jaya Catholic University of Indonesia, Jakarta, Indonesia; [4]Department of Microbiology, School of Medicine and Health Sciences, Atma Jaya Catholic University of Indonesia, Jakarta, Indonesia

*Corresponding author: mora.octavia@atmajaya.ac.id

## Abstract

Periodontal bone defects require bone grafting materials that provide structural stability, biocompatibility, and reliable biological performance. Synthetic alloplastic scaffolds composed of biphasic calcium phosphate, integrating hydroxyapatite (HAp) and β-tricalcium phosphate (β-TCP), offer a promising alternative to other graft materials. Polycaprolactone provides flexibility and support for pore formation, while copper (Cu) and zinc (Zn) ions contribute to their antimicrobial and osteogenic benefits. This study aimed to investigate the physicochemical, morphological, mechanical, and biological properties of a synthetic HAp40/β-TCP60 alloplastic scaffold reinforced with polycaprolactone and to compare them with those of a commercial xenograft. The scaffold was fabricated using a freeze-drying method with dimethylformamide, and characterization included Fourier-transform infrared spectroscopy (FTIR) and X-ray diffraction (XRD) for chemical and crystalline confirmation, Archimedes principle for porosity, light microscopy, and scanning electron microscopy (SEM) for morphological assessment, compressive testing, blood adhesion, as well as water and blood absorption analysis. FTIR and XRD verified the successful incorporation of polycaprolactone and the formation of a well-ordered biphasic calcium phosphate structure. Light microscopy showed that the synthetic scaffold had smaller macropore dimensions (324±49 µm) than the control (1410±541 µm), while SEM demonstrated markedly higher microporosity (8.184±2.581 µm) compared to the control (0.287±0.091 µm). Water absorption was lower in the synthetic scaffold (174.7%) than in the control (1172.5%), whereas blood absorption was comparable (300% vs 316.6%). The synthesized scaffold also exhibited superior blood adhesion, as evidenced by the absence of turbidity after agitation. Mechanical testing revealed that the control had superior compressive and yield strengths (0.980 MPa and 0.537 MPa, respectively) compared to the synthesized scaffold (0.287 MPa and 0.126 MPa, respectively). In conclusion, the synthetic HAp40/β-TCP60 scaffold exhibited properties within optimal ranges, highlighting its potential as a promising synthetic alloplastic material for clinical bone regeneration.

**Keywords**: Biphasic calcium phosphate, periodontitis, physiochemical characterization, porosity

## Introduction

Periodontitis is a chronic inflammatory disease characterized by progressive destruction of the tooth-supporting tissues, including the alveolar bone, periodontal ligament, and cementum,



https://narraj.org/

Received: November 28, 2025 - Accepted: January 23, 2026 - Published online: January 30, 2026

primarily due to bacterial infection and plaque accumulation [1]. Globally, periodontitis is a major oral health concern and is among the most prevalent non-communicable diseases, often leading to tooth loss and systemic complications such as cardiovascular disease [2,3]. In Indonesia, its high prevalence highlights the urgent need for effective and accessible therapeutic strategies.

Conventional periodontal therapies such as scaling, root planning, and surgical interventions can halt disease progression but rarely achieve complete regeneration of lost periodontal structures [4]. Bone grafting is therefore considered a key approach in periodontal regeneration, as it provides a scaffold that facilitates osteoblast adhesion, extracellular matrix deposition, and new bone formation [5,6]. Although autografts remain the gold standard due to their superior osteogenic and osteoconductive properties, their use is limited by donor-site morbidity, high cost, and limited availability [7]. These limitations have prompted the development of synthetic bone substitutes (alloplasts) as alternatives.

Among synthetic grafts, calcium phosphate ceramics, particularly hydroxyapatite (HAp) and β-tricalcium phosphate (β-TCP), are widely used due to their chemical and structural similarities to natural bone minerals [8]. However, HAp degrades slowly and exhibits brittleness, whereas β-TCP resorbs more rapidly and lacks long-term mechanical stability [8-10]. Biphasic calcium phosphate (BCP), composed of HAp and β-TCP, is designed to combine the advantages of both materials, offering a balance between structural stability and controlled resorption. Its bioactivity and resorption rate can be tailored by adjusting the HAp-to-β-TCP ratio, with previous studies demonstrating superior osteoconductivity compared with single-phase ceramics [11,12]. Moreover, because BCP is fully synthetic, it is readily available, avoiding donor-site morbidity and supply constraints associated with autograft or allograft materials [13]. In this study, a 40% HAp:60% β-TCP ratio was selected, as it has demonstrated favorable biological performance in previous studies [14].

To further enhance scaffold properties, polycaprolactone (PCL) was incorporated into the BCP matrix to improve mechanical integrity and structural flexibility, as pure calcium phosphate ceramics can be brittle. PCL provides a supportive polymeric framework that facilitates cell adhesion, proliferation, and differentiation [15]. Following polymer integration, the scaffold was additionally modified with copper (Cu) and zinc (Zn) ions to introduce biological functionality, as these trace elements regulate osteogenesis and provide antimicrobial effect [16-19]. Cu contributes to antimicrobial activity and promotes angiogenesis, while Zn inhibits biofilm production and prevents bone resorption [16,18]. The combined incorporation of PCL, Cu, and Zn is intended to produce a mechanically robust, biologically active, and antimicrobial BCP-based scaffold that not only mimics the structural characteristics of natural bone but also enhances regenerative potential compared with unmodified BCP ceramics.

Commercial xenografts are widely used as bone substitutes in Indonesia and internationally due to their close resemblance to human bone in terms of mineral composition and trabecular architecture [20]. The deproteinization process preserves their natural interconnected porosity and hydroxyapatite-rich structure, resulting in excellent osteoconductive properties and high biocompatibility [20-22]. As one of the most established and reliable biomaterials for bone regeneration, bovine xenografts serve as an appropriate benchmark for evaluating new synthetic grafts. For this reason, a commercially available bovine xenograft was selected as the control group in this study to enable a clinically relevant comparison and to assess whether the laboratory-fabricated BCP scaffolds can serve as dependable, cost-effective alternatives.

The success of a scaffold is influenced by factors such as porosity, surface chemistry, and mechanical strength. An ideal bone graft should exhibit high porosity with interconnected pores to support cell infiltration, vascularization, and nutrient diffusion while maintaining sufficient mechanical integrity [5,6]. Freeze-drying has emerged as an effective fabrication technique for producing three-dimensional porous structures, enabling control over pore architecture and interconnectivity [23]. Therefore, this study aimed to compare a freeze-dried BCP scaffold composed of 40% HAp and 60% β-TCP with a commercially available xenograft. The comparison was conducted based on physicochemical and biological properties, including porosity (evaluated using Archimedes' principle, scanning electron microscopy (SEM), and light microscopy), Fourier-transform infrared spectroscopy (FTIR), X-ray diffraction (XRD), water and blood absorption capacity, blood adherence, and mechanical strength. The results are expected to

provide insights into the potential of BCP scaffolds as a synthetic alternative for bone grafting applications in periodontal regeneration.

# Methods

## Fabrication of bone graft scaffold

PCL was dissolved in dimethylformamide at 50°C with a magnetic stirrer. HAp granules (Sigma Aldrich, St. Louis, USA) were initially dissolved in $HNO_3$ (Merck, Darmstadt, Germany). The ceramic powders were then gradually added to the PCL solution, followed by Cu (Sigma-Aldrich) and Zn (Sigma-Aldrich) powders, and stirred to homogenize. The mixtures were poured into silicone molds (20×20×40 mm), frozen at −80°C for 6 days, and subsequently freeze-dried using a CoolSafe™ freeze-dryer (Labogene, Allerød, Denmark) at −55°C for 48 h to remove solvents. The dried scaffolds were sterilized using a vacuum oven at room temperature (25°C) until characterization. To assess the effectiveness of the synthesized BCP scaffolds as a commercial bone graft material, commercially available BATAN® xenograft (Focustindo Cemerlang, Bogor, Indonesia) was used as the reference control. One replicate was prepared and evaluated for each sample.

## Fourier transform infrared spectroscopy (FTIR)

An IRTracer-100 FTIR (Shimadzu Corporation, Kyoto, Japan) was used to characterize the organic and inorganic functional groups present in the scaffold samples. The scaffolds were sliced into thin sheets prior to analysis. FTIR spectra were obtained within the range between 4000 and 400 $cm^{-1}$ using an IRTracer-100 spectrometer equipped with LabSolutions IR software (Shimadzu Corporation, Kyoto, Japan) and the Attenuated Total Reflectance (ATR) technique.

## X-ray diffraction (XRD)

The crystal phases of the scaffolds were verified using X-ray diffraction (Malvern PANanalytical's Aeris, Almelo, Netherlands) with a monochromatic CuKa radiation (λ=1.5406 Å) over the 2θ range of 5–89.99°. The operation voltage and current were 40kV and 30 mA, respectively. The data were analyzed using X'Pert Quantify software (Malvern PANalytical, Almelo, Netherlands), and the collected data were identified by comparison with International Centre for Diffraction Data (ICDD) references.

## Porosity assessment using Archimedes' principle

The porosity of the scaffolds was assessed using the liquid displacement method based on Archimedes' principle. The scaffold was cut into a 1 cm x 1 cm square, submerged in phosphate-buffered saline (PBS), and the submerged weight ($m_{sub}$) was recorded using an analytical balance. The sample was then fully submerged in PBS for 15 minutes, and the saturated weight (msat) was measured. The scaffolds were vacuum-dried at 27 °C for 24 and the dry mass was measured ($m_{dry}$). The open porosity (γ, %) was calculated according to Equation (1) [24].

$$\gamma\,(\%) = \frac{m_{sat} - m_{dry}}{m_{sat} - m_{sub}}\, x\, 100 \qquad (1)$$

where γ represents the percentage of open porosity; $m_{dry}$ is the dry mass; $m_{sat}$ is the saturated mass, and $m_{sub}$ is the submerged mass.

## Macropore assessment using light microscopy

The morphology of the scaffolds was examined using an Olympus CX-23 light microscope (Olympus Corporation, Tokyo, Japan) to evaluate macropore size and surface morphology. The scaffolds were sliced into sheets and observed under 10× magnification, and digital micrographs were captured for further analysis. The pore diameter and distribution were calculated from the light microscopy images using ImageJ software (National Institutes of Health, Bethesda, USA) by selecting five macropores for measurement.

### Scanning electron microscopy (SEM)

The surface morphology and micropore structure of the bone graft scaffolds were examined using Field Emission Scanning Electron Microscopy (JEOL JSM-6510LA, JEOL Ltd., Tokyo, Japan). The samples were cut into squares measuring approximately 1×1 cm, mounted on aluminum stubs using carbon tape, and the cross-sections of the porous scaffolds were coated with a thin layer of gold using a sputter coater to prevent imaging artifacts from electrical charging. SEM imaging was performed at an accelerating voltage of 10 kV, and images were captured at magnifications ranging from 2500× to 25000×. The pore size was calculated from the SEM images using ImageJ software (National Institutes of Health, Bethesda, USA) by selecting five micropores for measurement.

### Mechanical characterization of the scaffold

The mechanical properties of the scaffolds were assessed using uniaxial compression testing. Cylindrical scaffold specimens were prepared and subjected to compression using a custom-built universal testing machine operated at a constant crosshead speed of approximately 10 µm/s, with a maximum load capacity of 20.25 kN [25]. Prior to testing, the instrument was calibrated to ensure measurement accuracy. The testing apparatus was identical in design and technical specifications to the system previously described [25]. The ultimate compressive strength and yield strength ($\sigma_\gamma$) were determined from the resulting stress–strain curves and expressed in megapascals (MPa). The ultimate compressive strength was defined as the maximum stress sustained by the material before failure, while the yield strength was determined by constructing two tangent lines to the curve and locating their intersection point [26].

### Water absorption

Both samples were cut into 1 cm × 1 cm squares and weighed to obtain their initial dry weight ($W_o$), then immersed in 20 mL of deionized water at room temperature (25°C) for 1 hour. After immersion, the specimens were gently removed, blotted with filter paper to eliminate surface water, and weighed again to record the wet weight ($W_t$). The water absorption rate was calculated using the equation of $W\ (\%) = ((W_t-W_o)/W_o)\ x100$ [27]; where W represents the water absorption rate after a specific time period; $W_t$ is the weight after submerged in water, and $W_o$ is the initial dry weight.

### Blood absorption and adherence

Both specimens were cut into squares measuring approximately 10 mm × 10 mm. A volume of 200 µL of fresh sheep blood, previously mixed with 3.8% sodium citrate solution to prevent coagulation, was dropped onto each specimen and left for 1 hour to allow absorption. The specimens were weighed before ($D_o$) and after blood exposure ($D_t$), and all changes were documented. The blood absorption capacity was calculated using the equation of $Q\ (\%) = ((D_t-D_o)/D_o)\ x100$ [27]; where $D_o$ represents the initial dry weight of the specimen, and $D_t$ represents the weight after blood absorption. Following this, each specimen was placed in a test tube containing 40% PBS, shaken 10 times, and documented to assess blood adhesion on the scaffold surface.

## Results

### Physical appearance of the scaffold

A noticeable difference was observed between the control and the HAp40/β-TCP60/PCL/Cu/Zn scaffold. The control exhibited a rigid structure with large, uniformly distributed pores. In contrast, the alloplastic scaffold showed smaller, less distinct pores and a spongy consistency (**Figure 1A**). The HAp40/β-TCP60/PCL/Cu/Zn scaffold also appeared more brittle and exhibited a smooth surface (**Figure 1B**).

### Fourier transform infrared spectroscopy (FTIR) results

Both FTIR spectra of the control specimen and the HAp40/β-TCP60/PCL/Cu/Zn scaffold displayed the presence of the phosphate functional group of calcium phosphate. The $v_3\ PO_4^{3-}$ stretching bands appeared at 1041.57 $cm^{-1}$ and 1057.00 $cm^{-1}$, accompanied by the $v_4$ bending

modes within the 700–500 $cm^{-1}$ region. These signals were further supported by the presence of the v1 symmetric stretching peak near 962–965 $cm^{-1}$ and the v2 bending band observed between 400–460 $cm^{-1}$, confirming the expected phosphate profile in both materials. In addition to these bands, the control specimen exhibited prominent absorptions at 1651.07 $cm^{-1}$ and 1543.06 $cm^{-1}$ corresponding to the amide I and amide II regions of collagen, which are typically found in natural bone. Meanwhile, the HAp40/β-TCP60/PCL/Cu/Zn scaffold showed additional absorptions in the 1700–1500 $cm^{-1}$ range associated with the carbonate functional groups of PCL (**Table 1**).

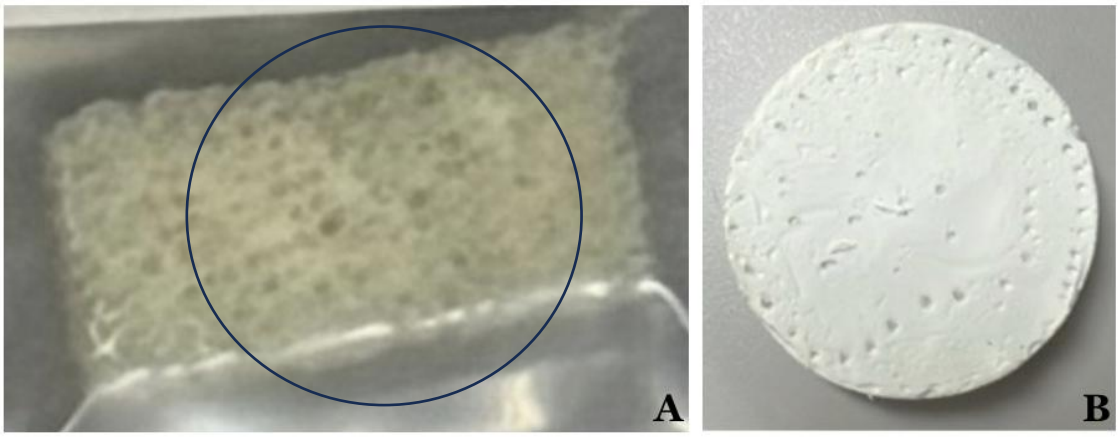


Figure 1. Comparison of physical appearance of scaffolds between commercially available xenograft as a control (a) and HAp40/β-TCP60/PCL/Cu/Zn scaffold.

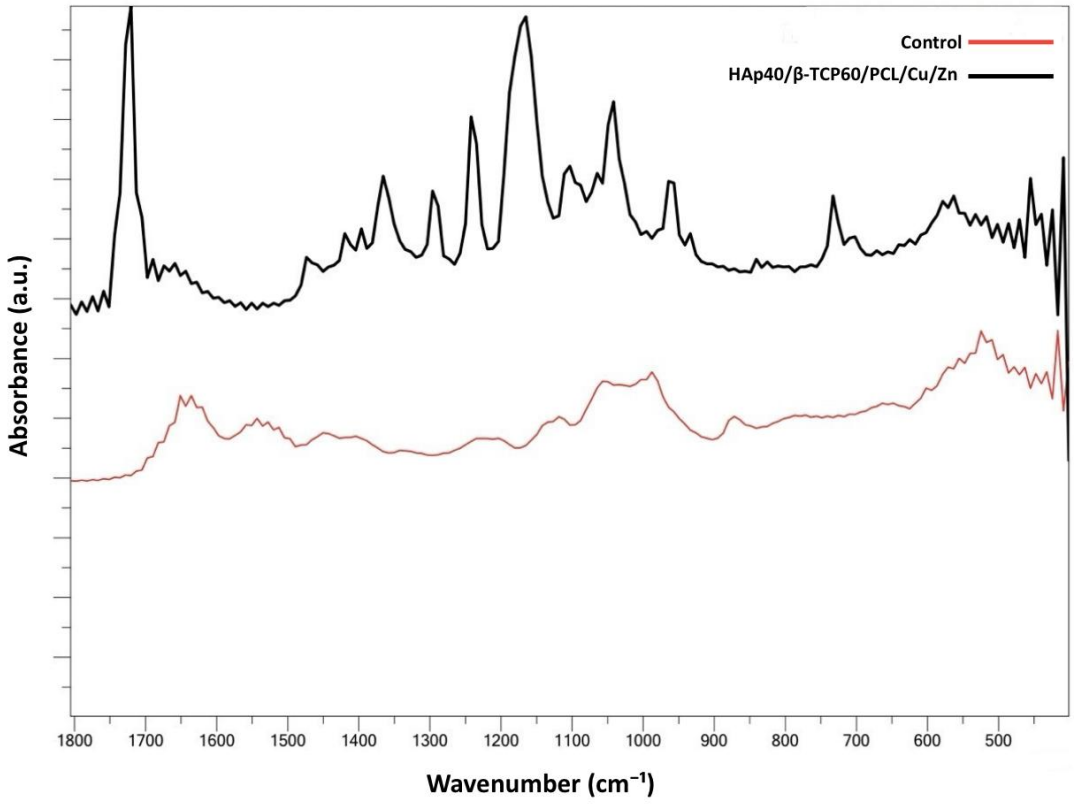


Figure 2. FTIR profile comparison between the xenograft control (red) and HAp40/β-TCP60/PCL/Cu/Zn scaffold (black).

Table 1. Summary of functional groups and corresponding FTIR peaks of HAp40/β-TCP60/PCL/Cu/Zn and control scaffolds

| No | Control | | | HAp40/β-TCP60/PCL/Cu/Zn | | |
|---|---|---|---|---|---|---|
| | Wavelength | Stretching | Functional group | Wavelength | Stretching | Functional group |
| 1 | 1651.07 $cm^{-1}$ | C=O | Amide I | 1720.51 $cm^{-1}$ | C=O | Carbonate |
| 2 | 1543.06 $cm^{-1}$ | C-N-H | Amide II | 1165.01 $cm^{-1}$ | C–O–C | Carbonate |
| 3 | 1057.00 $cm^{-1}$ | P–O | Phosphate (ν3) | 1242.16 $cm^{-1}$ | C–O–C | Carbonate |
| 4 | 987.56 $cm^{-1}$ | P–O | Phosphate (ν1) | 1041.57 $cm^{-1}$ | P–O | Phosphate (ν3) |
| 5 | 871.83 $cm^{-1-}$ | P–O | Phosphate (ν1) | 964.41 $cm^{-1}$ | P–O | Phosphate (ν1) |
| 6 | 524.64 $cm^{-1}$ | P–O | Phosphate (ν4) | 732.96 $cm^{-1}$ | P–O | Phosphate(ν4) |
| 7 | 416.63 $cm^{-1}$ | P–O | Phosphate (ν2) | 455.21 $cm^{-1}$ | P–O | Phosphate (ν2) |
| 8 | 401.20 $cm^{-1}$ | P–O | Phosphate (ν2) | 408.92 $cm^{-1}$ | P–O | Phosphate (ν2) |

## X-ray diffraction (XRD) results

The control material displayed multiple broad reflections characteristic of biological hydroxyapatite, with identifiable peaks at 2θ=21.01°, 11.73°, and 29.35° (**Table 2**). Phase analysis confirmed the presence of two crystalline phases: hydroxyapatite, with a density of 3.215 g/cm³, a fractional volume of 55.4%, and a fractional weight of 63.4%; and brushite, with a density of 2.312 g/cm³, a fractional volume of 44.6%, and a fractional weight of 36.6%. In contrast, the synthesized HAp40/β-TCP60%/PCL/Cu/Zn scaffold exhibited three dominant and sharper reflections at 2θ=21.33°, 23.64°, and 26.50°, corresponding to the (–202), (031), and (–132) crystal planes (**Table 2**). Phase identification revealed a single crystalline phase of calcium phosphorous oxide, with a density of 2.467 g/cm³ and a fractional volume and weight of 100%, indicating complete phase uniformity in the synthesized scaffold.

Table 2. Crystallographic parameters derived from X-ray diffraction (XRD) analysis of HAp40/β-TCP60/PCL/Cu/Zn and control scaffolds

| Parameter | Control | HAp40/β-TCP60/PCL/Cu/Zn |
|---|---|---|
| Miller indices (hkl) | (0 2 1), (0 2 0), (0 4 1) | (-2 0 2), (0 3 1), (-1 3 2) |
| 2θ (°) | 21.0152; 11.7252; 29.3542 | 21.3252; 23.6403; 26.4990 |
| Interplanar d-spacing (Å) | 4.224; 7.541; 3.040 | 4.163; 3.760; 3.361 |
| Height (%) | 100; 88.38; 66.04 | 100; 47.70; 8.24 |

## Porosity assessment results based on Archimedes' principle

Porosity analysis using Archimedes' principle revealed that the control scaffold had a markedly higher total porosity (95.79%) compared with the synthesized scaffold (69.88%) (**Figure 3**), indicating increased structural densification following scaffold modification.

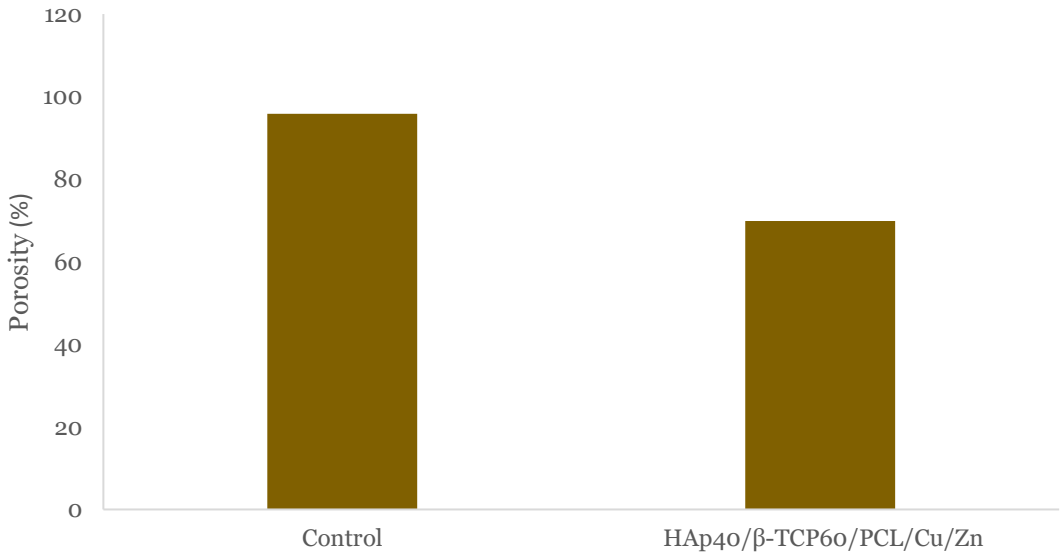


Figure 3. Porosity analysis using Archimedes principle of HAp40/β-TCP60/PCL/Cu/Zn and control scaffolds.

## Light microscopy assessment results

The control specimen exhibited large, well-defined macropores with rounded to oval shapes (**Figure 4A**). Based on the measurement of five representative pores, the macropore dimensions varied widely, ranging from 985 µm to 6086 µm, with an average size of 2539±2047 µm. The macropores were separated by relatively thick scaffold walls. In contrast, HAp40/β-TCP60/PCL/Cu/Zn scaffold appeared denser under microscopic observation (**Figure 4B**). The macropores did not form open cavities as seen in the control, but instead appeared as narrow slit-like spaces distributed throughout the field of view. These slit-like pores showed irregular shapes formed between polymer fibers, with sizes ranging from 286 µm to 396 µm, with an average size of 324±49 µm.

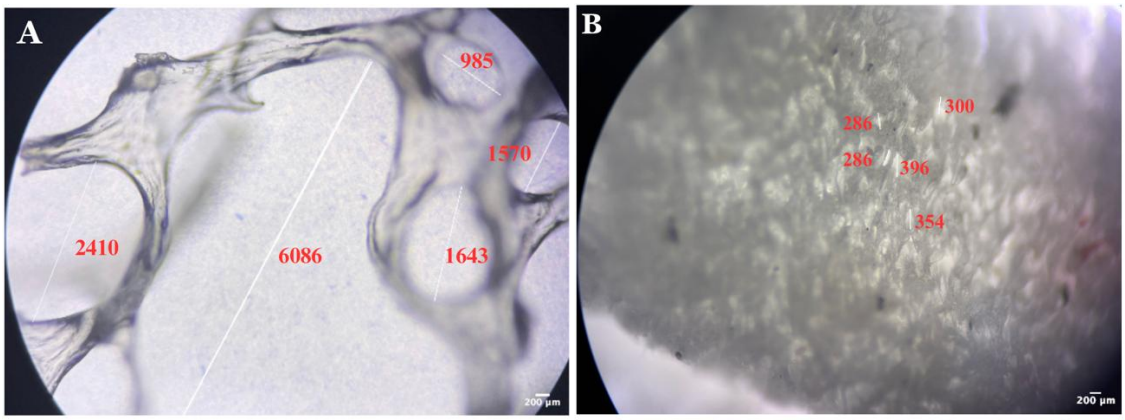


Figure 4. Representative light microscopy images at 10× magnification with five pores measured per group: (A) control, (B) HAp40/β-TCP60/PCL/Cu/Zn.

## Scanning electron microscope (SEM) results

The control exhibited a compact morphology characterized by a fibrillar collagen-like pattern with submicron pores, typical of natural trabecular bone architecture (**Figure 5A**). Quantitative analysis of five micropores showed that the control possessed minimal microporosity, with an average micropore size of 0.287±0.091 µm. In contrast, the synthesized scaffold exhibited a distinctly porous architecture with a more uniform, interconnected micropore distribution (**Figure 5A**). At low magnification (2500×), the synthesized scaffold revealed micropores ranging from 5–12 µm, yielding an overall average micropore size of 8.184±2.581 µm, measured from five micropores. At higher magnification (25000×), the scaffold showed pore walls with sharp edges, irregular contours, and variable thicknesses arranged in multiple layers. The pore walls appeared generally smooth, with visible polymer fibers integrated throughout the structure. Thin, elongated polymeric filaments bridging adjacent pores were also observed, indicating the formation of a connected microstructural network within the scaffold (**Figure 5B**).

## Mechanical characterization of the scaffold

The mechanical properties of the HAp40/β-TCP60/PCL/Cu/Zn scaffold differed from those of the control specimen (**Figure 6**). The control specimen exhibited an ultimate compressive strength of 0.980 MPa and a yield strength of 0.537 MPa. In contrast, the HAp40/β-TCP60/PCL/Cu/Zn scaffold showed lower values, with an ultimate compressive strength of 0.287 MPa and a yield strength of 0.126 MPa.

## Water and blood absorption analysis results

HAp40/β-TCP60/PCL/Cu/Zn scaffold exhibited a water absorption capacity of 174.7% and a blood absorption capacity of 300%, whereas the control specimen demonstrated markedly higher water absorption at 1172.5% and a slightly higher blood absorption of 316.6% (**Figure 7**).

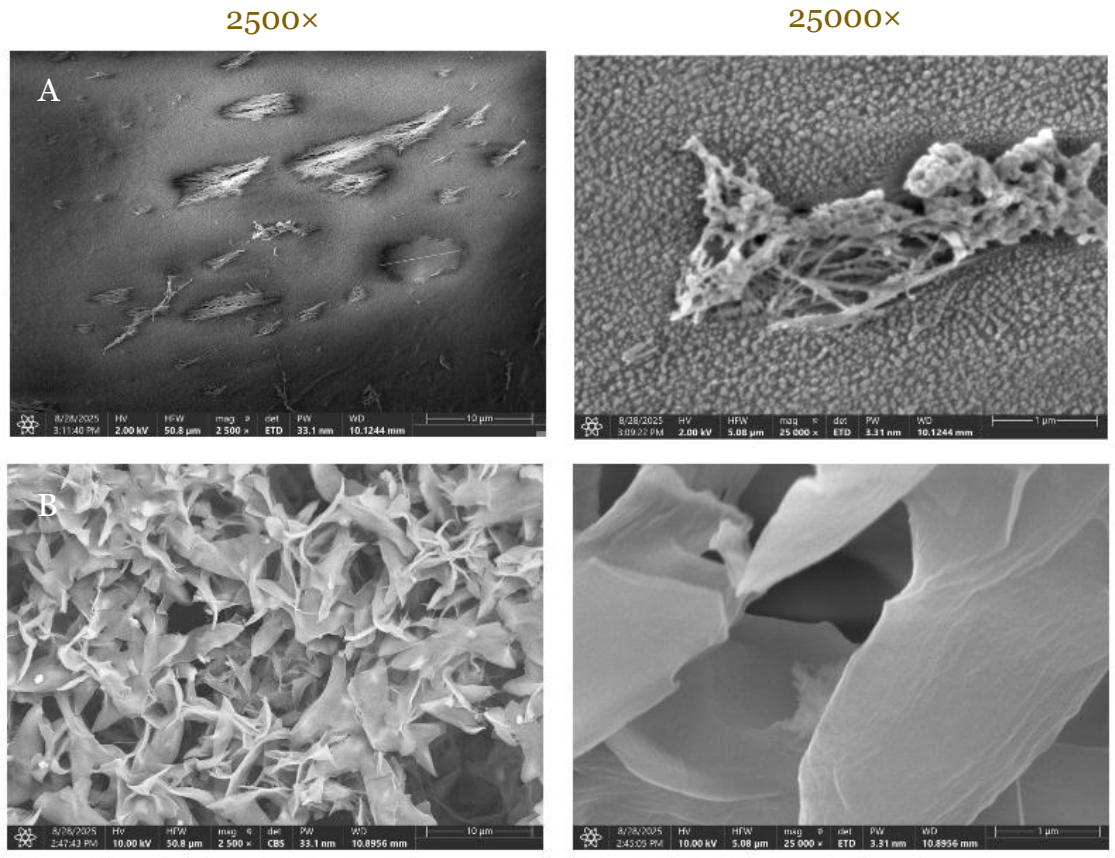


Figure 5. Scanning electron microscope (SEM) results showing morphology characteristics of (A) control and (B) HAp40/β-TCP60/PCL/Cu/Zn scaffolds.

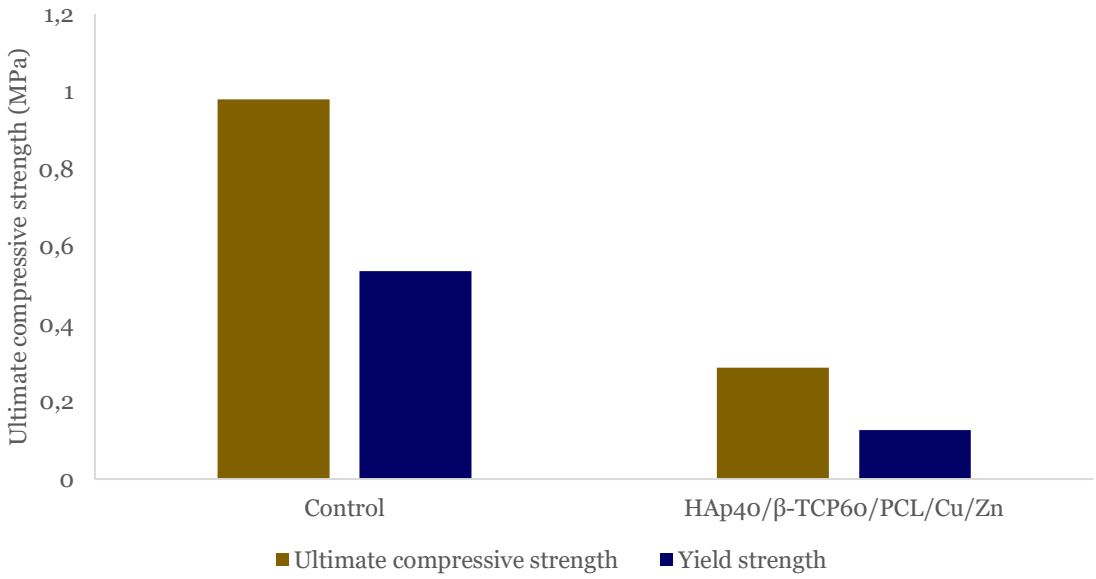


Figure 6. Ultimate compressive strength and yield strength of HAp40/β-TCP60/PCL/Cu/Zn and control scaffolds.

## Blood adherence assessment results

The control scaffold demonstrated poor blood adhesion, as indicated by the change in color of the surrounding phosphate-buffered solution from clear to bright red after shaking (**Figure 8A**). In contrast, the HAp40/β-TCP60/PCL/Cu/Zn scaffold showed stronger blood retention, with minimal change in solution color before and after 10 shaking cycles (**Figure 8B**).

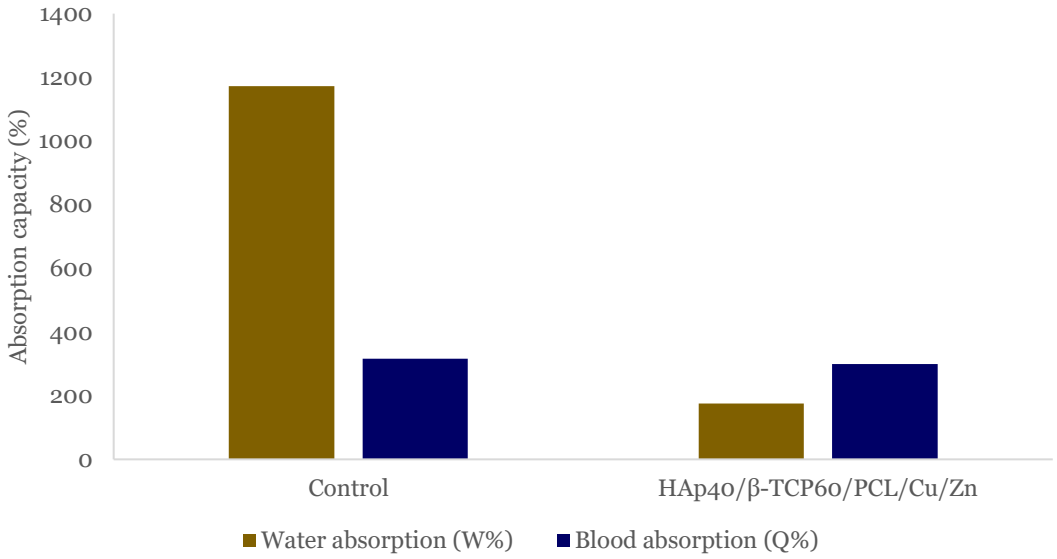


Figure 7. Water absorption and blood absorption capacity of HAp40/β-TCP60/PCL/Cu/Zn and control scaffolds.

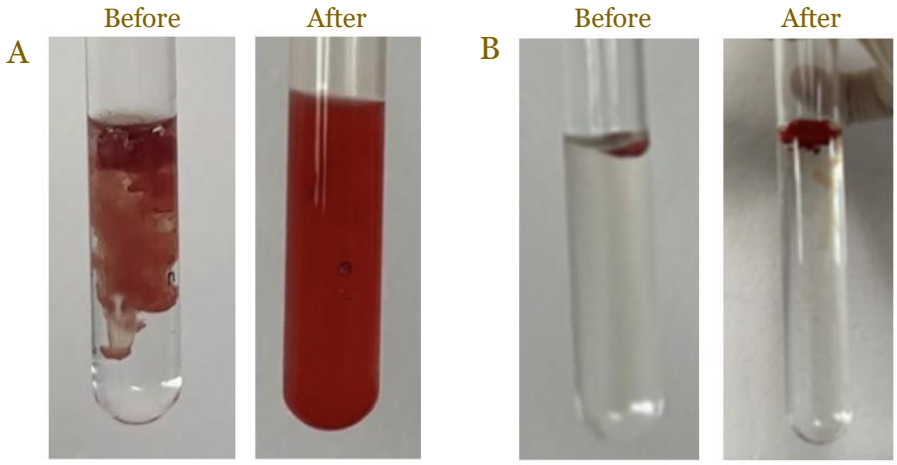


Figure 8. Blood adhesion test before and after being shaken 10 times in PBS of (A) control and (B) HAp40/β-TCP60/PCL/Cu/Zn scaffolds.

## Discussion

The comparative characterization of the control and the synthesized HAp40/β-TCP60/PCL/Cu/Zn scaffold revealed fundamental differences in chemical composition, crystalline structure, pore architecture, mechanical performance, and biological interaction. FTIR and XRD analyses provide the first indication of this contrast. Both materials displayed the characteristic phosphate vibrational modes (v1–v4), confirming a calcium phosphate base [28]. However, the control showed distinct amide I and amide II bands at 1651.07 $cm^{-1}$ and 1543.06 $cm^{-1}$, corresponding to collagen, an organic component naturally present in bone [29]. Meanwhile, the synthetic material exhibited ester bands attributed to PCL, reflecting its engineered polymer–ceramic composition. These qualitative chemical differences were mirrored by their crystalline profiles. XRD analysis showed that the xenograft control consisted of hydroxyapatite and brushite phases with varying densities and fractional contributions, reflecting the heterogeneity of biological mineralization. The synthesized scaffold, on the other hand, displayed a single uniform crystalline phase, calcium phosphorous oxide, with 100% fractional volume and weight. The sharp, well-defined diffraction peaks of the scaffold indicate a highly ordered mineral phase formed under controlled fabrication conditions, in contrast to the broader peaks typical of natural bone apatite.

These fundamental compositional and mineralogical differences strongly influenced the materials' pore architecture. The control maintained its natural trabecular structure, resulting in a high measured porosity of 95.79% and large, rounded macropores ranging from 936 to 6086 μm. In comparison, the HAp40/β-TCP60/PCL/Cu/Zn scaffold exhibited a lower porosity of 69.88%. This difference is also reflected in the scaffold's physical appearance: the control exhibited large, uniform pores, while the synthesized scaffold showed less distinct pores. This reflects how each material forms its pore network. Natural bone retains its interconnected trabeculae and voids, while the synthetic scaffold relies on solvent crystallization during freeze-drying to generate porosity. Dimethylformamide has a melting point of −61°C, which is below the freeze-drying temperature (−55°C). Therefore, this causes the solvent to be unable to fully crystallize, resulting in limited ice crystal formation and ultimately reduced pore generation. Similar outcomes were observed in previous studies, highlighting the importance of solvent crystallization in pore development [30,31]. The higher β-TCP content in the scaffold may modestly contribute to porosity due to its highly resorbable nature [10]. A similar finding was previously reported, showing that an increase in β-TCP content led to higher porosity [32].

Although the porosity of the synthesized scaffold is lower than that of the control, the overall porosity remains within the optimal 60–70% range reported to balance mechanical integrity and osteoconductivity [33]. Light microscopy supported these findings, showing that the HAp40/β-TCP60/PCL/Cu/Zn scaffold formed narrow, slit-like pores (286–396 μm) rather than large, open cavities. Importantly, the slit-like pore range falls within the 250–400 μm window considered optimal for osteoblast proliferation and angiogenesis, whereas pores exceeding 500 μm may compromise effective cell attachment and early mechanical stability [34,35]. The denser pore morphology of the scaffold can also be attributed to the high viscosity of the PCL/dimethylformamide solution during freeze-drying, which further limits ice crystal growth and restricts macropore expansion [36].

SEM analysis provided insight into the microstructural differences. The control exhibited a fibrillar collagen-like network with submicron pores (<1 μm), consistent with trabecular bone's natural microstructure, which enhances protein adsorption and cell anchorage. In contrast, the synthesized scaffold contained uniformly distributed micropores measuring 5–12 μm, with an average micropore diameter of 8.184±2.581 μm, larger than the xenograft's 0.287±0.091 μm. These micropores were interconnected by thin polymeric filaments and bordered by multilayered pore walls with sharp edges and irregular contours. This hierarchical arrangement indicates successful integration of ceramic and polymer phases, yielding a multi-scale porous network capable of supporting both mechanical stability and cellular infiltration. The pores <10 μm increase surface area, enhancing ion exchange, protein adsorption, and osteogenic cell attachment, while interconnected microchannels facilitate tissue continuity across the scaffold [37]. The scaffold's combination of macropores within the osteogenic range and micropores conducive to protein interaction suggests a favorable environment for early cell colonization.

The difference in porosity is also reflected in the water and blood absorption test. The control had a high-water absorption (1172.5%), reflecting its collagen-rich, high-porosity structure, while the HAp40/β-TCP60/PCL/Cu/Zn sample had lower water absorption (174.7%) due to its smoother surface and the hydrophobic nature of PCL, whose non-polar backbone restricts water penetration [38]. Despite this, both materials showed comparable blood absorption (300% *vs* 316.6%), though the mechanism differed. The synthesized scaffold relied more on capillary action within its microporous network to retain blood, whereas the xenograft control absorbed blood through its larger, more open voids [39]. The blood adhesion test revealed the scaffold's markedly superior ability to retain blood, which is indicated by the PBS surrounding the scaffold remaining unchanged after shaking, whereas the control released blood readily into the solution. This selective retention of viscous fluids, such as blood, aligns with evidence suggesting that smaller and interconnected pores enhance capillary forces [39]. Effective blood adhesion is crucial for early clot stabilization, angiogenesis initiation, and overall regenerative success, suggesting that the synthetic scaffold may provide a more favorable early-healing environment [40].

Additionally, the control exhibited higher compressive performance, with an ultimate compressive strength of 0.980 MPa and a yield strength of 0.537 MPa, compared with the lower values observed for the scaffold (0.287 MPa and 0.126 MPa, respectively). This can be attributed

to the xenograft's dense trabecular walls and its hydroxyapatite-rich mineral phase, whereas the synthetic scaffold incorporates a higher proportion of β-TCP, a brittle ceramic known to reduce compressive strength at higher ratios [10,41]. Despite differences in mechanical properties, both materials exhibited elastic–plastic behavior, indicating sufficient ductility to withstand deformation before failure. This characteristic helps preserve pore architecture during early regeneration and contributes to a supportive cellular environment [42]. Both scaffolds fall within the accepted mechanical range for non-load-bearing dental bone augmentation (0.1–16 MPa), confirming their suitability for alveolar and peri-implant applications [43].

Altogether, while the control maintains superior natural porosity and trabecular fidelity, the HAp40/β-TCP60/PCL/Cu/Zn scaffold offers a more controlled, reproducible architecture with ideal pore dimensions, uniform crystallinity, adequate mechanical stability, and strong hemoadhesive behavior. These combined characteristics position the synthesized scaffold as a promising bone graft material that balances biological performance with structural integrity approaching the profile of an ideal engineered bone substitute suitable for clinical applications where predictable behavior, controlled resorption, and early blood-mediated integration are essential.

## Conclusion

The HAp40/β-TCP60/PCL/Cu/Zn scaffold exhibited a balanced combination of structural, mechanical, and biological properties suitable for use as a synthetic graft in dental bone augmentation. FTIR and XRD confirmed the presence of an ordered biphasic calcium phosphate phase with retained PCL components, while microscopic analyses showed a consistent microporous network. Although its mechanical strength was lower than that of the xenograft control, both remained within the range required for non-load-bearing sites. Notably, the scaffold demonstrated strong blood retention and comparable blood absorption, indicating superior hemocompatibility and potential to support early angiogenesis. These results collectively highlight the scaffold as a viable and stable alternative to xenograft materials for clinical bone regeneration.

### Ethics approval

The study protocol was approved by Atma Jaya Catholic University of Indonesia, Jakarta, Indonesia.

### Acknowledgments

The authors would like to express their gratitude to Atma Jaya Catholic University of Indonesia for funding the research and providing laboratory facilities and technical assistance during this research.

### Competing interests

All the authors declare that there are no conflicts of interest.

### Funding

This study received external funding from Atma Jaya Catholic University of Indonesia.

### Underlying data

Derived data supporting the findings of this study are available from the corresponding author on request.

### Declaration of artificial intelligence use

We hereby confirm that no artificial intelligence (AI) tools or methodologies were utilized at any stage of this study, including during data collection, analysis, visualization, or manuscript preparation. All work presented in this study was conducted manually by the authors without the assistance of AI-based tools or systems.

## How to cite

Novelia D, Cahyadi TO, Sidharta NMP, *et al.* Development and evaluation of a synthetic Cu-Zn-reinforced biphasic calcium phosphate scaffold for periodontal bone repair. Narra J 2026; 6 (1): e3001 - http://doi.org/10.52225/narra.v6i1.3001.

## References

1. Goddard M, Smith P. Equity of access to health care services: theory and evidence from the UK. Soc Sci Med 2001;53(9):1149-1162.
2. Wijaksana IKE. Periodontal chart dan periodontal risk assessment sebagai bahan evaluasi dan edukasi pasien dengan penyakit periodontal. J Kesehat Gigi 2019;6(1):19.
3. Mehrotra N, Singh S. Periodontitis. Treasure Island: StatPearls Publishing; 2023.
4. Kwon T, Lamster IB, Levin L. Current concepts in the management of periodontitis. Int Dent J 2021;71(6):462-476.
5. Hutama AS, Nugroho A. Optimasi pembuatan scaffold dengan struktur pori-pori beraturan menggunakan metode response surface method. J Mater Pros Manuf 2020;4(1):1-11.
6. Filda N, Triviana N, Nathania A, Saputro. Identification of calcium and phosphate content in chicken bones and duck bones. Science, engineering, and technology. Nusant Sci Technol Proc 2021;11(12):35-39.
7. Zhang J, Li S, He H, et al. Clinical guidelines for indications, techniques, and complications of autogenous bone grafting. Chin Med J 2024;137(1):5-7.
8. Habibah TU, Salisbury HG. Hydroxyapatite Dental Material PubMed. Treasure Island: StatPearls Publishing; 2020.
9. Family R, Solati-Hashjin M, Namjoy Nik S, Nemati A. Surface modification for titanium implants by hydroxyapatite nanocomposite. Caspian J Intern Med 2012;3(3):460-465.
10. Rodríguez VR, Gonzales APG, Avila JG, Caballero AD. Use of beta-tricalcium phosphate bone graft in dental implants for bone regeneration. Bionorte. 2022;11(1):182–189.
11. Pae HC, Kang JH, Cha JK, *et al.* Bone regeneration using three-dimensional hexahedron channel structured BCP block in rabbit calvarial defects. J Biomed Mater Res B Appl Biomater 2019;107(7):2254-2262.
12. Titsinides S, Agrogiannis G, Karatzas T. Bone grafting materials in dentoalveolar reconstruction: A comprehensive review. Jpn Dent Sci Rev 2019;55(1):26-32.
13. Liu J, Guo X, Che Q, Su Z. Chitosan-oligosaccharide-bearing biphasic calcium phosphate bone cement: Preparation and angiogenic activity in vitro. Molecules 2025;30(11):2286.
14. Lee JH, Ryu MY, Baek HR, *et al.* Fabrication and evaluation of porous beta-tricalcium phosphate/hydroxyapatite (60/40) composite as a bone graft extender using rat calvarial bone defect model. ScientificWorldJournal 2013;2013:481789.
15. Raoufinia R, Hashemi S, Arabi K, *et al.* Poly ε-Caprolactone Scaffolds: Advancements in Bone Regeneration and Grafting. OBM Transplant 2025;9(02):1-8.
16. Ressler A, Žužić A, Ivanišević I, *et al.* Ionic substituted hydroxyapatite for bone regeneration applications: A review. Open Ceram 2021;6:100122:1-13.
17. Shen Q, Qi Y, Kong Y, *et al.* Advances in copper-based biomaterials with antibacterial and osteogenic properties for bone tissue engineering. Front Bioeng Biotechnol 2022;9:795425.
18. O'Connor JP, Kanjilal D, Teitelbaum M, *et al.* Zinc as a therapeutic agent in bone regeneration. Materials 2020;13(10):2211.
19. Esfahanizadeh N, Nourani MR, Bahador A, *et al.* The anti-biofilm activity of nanometric zinc doped bioactive glass against putative periodontal pathogens: an in vitro study. Biomed Glass 2018;4(1):95–107.
20. Naini AY, Kobravi S, Jafari A, *et al.* Comparing the effects of Bone+B® xenograft and InterOss® xenograft bone material on rabbit calvaria bone defect regeneration. Clin Exp Dent Res 2024;10(3):e875.
21. Amini Z, Lari R. A systematic review of decellularized allograft and xenograft-derived scaffolds in bone tissue regeneration. Tissue Cell 2021;69:101494.
22. Ferraz MP. Bone grafts in dental medicine: An overview of autografts, allografts and synthetic materials. Materials 2023;16(11):4117.
23. Capuana E, Lopresti F, Carfì Pavia F, *et al.* Solution-Based Processing for Scaffold Fabrication in Tissue Engineering Applications: A Brief Review. Polymers 2021;13(13):2041.
24. ang IN, Ahn YS. The Study of Copper Powder Sintering for Porous Wick Structures with High Capillary Force. Materials 2023;16(12):4231.

25. Manalu FRG, Basuki WW. Rancang bangun alat uji kekuatan material polimer dan komposit polimer berpenguat serat alam. Cylinder 2025;7(11):30-35.
26. Callister WD. Materials Science and Engineering: An Introduction. 10th ed. Salt Lake: Wiley; 2018.
27. Rozykulyyeva L, Widiyanti P, Astuti SD. Pomegranate-peel-chitosan-gelatin composite: A hemostatic dental sponge with antibacterial enhancement. Dent J 2025;58(2):171-179.
28. Dumitrescu CR, Neacsu IA, Surdu VA, *et al.* Nano-hydroxyapatite vs. Xenografts: synthesis, characterization, and in vitro behavior. Nanomaterials 2021;11(9):2289.
29. Abdul Rahman FS, Abdullah AM, Radhi A, *et al.* Physicochemical characterization of thermally processed goose bone ash for bone regeneration. J Funct Biomater 2023;14(7):351.
30. Ko YG. Formation of oriented fishbone-like pores in biodegradable polymer scaffolds using directional phase-separation processing. Sci Rep 2020;10(1):14472.
31. Aboudzadeh N, Khavandi A, Javadpour J, *et al.* Effect of dioxane and n-methyl-2-pyrrolidone as a solvent on biocompatibility and degradation performance of plga/nha scaffolds. Iran Biomed J 2021;25(6):408-416.
32. Bahir MM, Rajendran A, Pattanayak D, Lenka N. Fabrication and characterization of ceramic-polymer composite 3D scaffolds and demonstration of osteoinductive propensity with gingival mesenchymal stem cells. RSC Advances 2023;13(38):26967–26982.
33. Lee JH, Yi GS, Lee JW, Kim DJ. Physicochemical characterization of porcine bone-derived grafting material and comparison with bovine xenografts for dental applications. J Periodontal Implant Sci 2017;47(6):388-401.
34. Ramírez-Ruiz F, Núñez-Tapia I, Piña-Barba MC, *et al.* Polycaprolactone for hard tissue regeneration: Scaffold design and in vivo implications. Bioengineering. 2025 Jan 8;12(1):46.
35. Murphy CM, Haugh MG, O'Brien FJ. The effect of mean pore size on cell attachment, proliferation and migration in collagen-glycosaminoglycan scaffolds for bone tissue engineering. Biomaterials 2010;31(3):461-466.
36. Chen JS, Tu SL, Tsay RY. A morphological study of porous polylactide scaffolds prepared by thermally induced phase separation. J Taiwan Inst Chem Eng 2010;41(2):229-238.
37. Abbasi N, Hamlet S, Nguyen N. Porous scaffolds for bone regeneration. J Sci Adv Mater Devices 2020;5(1):1-9.
38. aseri R, Fadaie M, Mirzaei E, *et al.* Surface modification of polycaprolactone nanofibers through hydrolysis and aminolysis: a comparative study on structural characteristics, mechanical properties, and cellular performance. Sci Rep 2023;13(1):9434
39. Yusof AA bin M, Januddi MAFMS, Isa KM, *et al.* The effect of porosity and contact angle on the fluid capillary rise for bone scaffold wettability and absorption. Malays J Med Health Sci 2022;18(6):6-11.
40. Sanz M, Dahlin C, Apatzidou D, *et al.* Biomaterials and regenerative technologies used in bone regeneration in the craniomaxillofacial region: Consensus report of group 2 of the 15th European Workshop on Periodontology on Bone Regeneration. J Clin Periodontol 2019;46(21):82-91.
41. Juan PK, Fan FY, Lin WC, *et al.* Bioactivity and bone cell formation with poly-ε-caprolactone/bioceramic 3d porous scaffolds. Polymers 2021;13(16):2718.
42. Yusof Aabm, Isa Km, Szali Mafm, *et al.* Fracture characteristics of pla synthetic bone scaffolds with different specimen porosities. J Eng Sci Technol 2023;18(5):2493-2506.
43. Sunarso S, Suryadi A, Indrani DJ, Pangesty AI. Compressive strength of newly developed nonsintered hydroxyapatite blocks for bone graft applications. Eur J Dent 2024;18(3):815-819.